

Geophysical Research Letters®

RESEARCH LETTER

10.1029/2023GL104693

Key Points:

- We derive a complete series of coseismic deformation maps and detailed slip distribution of the 2023 Kahramanmaraş earthquakes
- The $M_w 7.7$ event produced normal dip-slip (~ 6 m) near the Goksun releasing bend and thrust dip-slip (~ 2 m) on the Dogansehir fault
- The coseismic slip behaviors on the Cardak and Pazarcik faults correlate with the interseismic kinematics

Supporting Information:

Supporting Information may be found in the online version of this article.

Correspondence to:

G. Feng,
fredgps@csu.edu.cn

Citation:

He, L., Feng, G., Xu, W., Wang, Y., Xiong, Z., Gao, H., & Liu, X. (2023). Coseismic kinematics of the 2023 Kahramanmaraş, Turkey earthquake sequence from InSAR and optical data. *Geophysical Research Letters*, 50, e2023GL104693. <https://doi.org/10.1029/2023GL104693>

Received 24 MAY 2023

Accepted 30 JUL 2023

Author Contributions:

Data curation: Lijia He, Guangcai Feng

Formal analysis: Lijia He, Guangcai Feng, Wenbin Xu, Yuedong Wang, Zhiqiang Xiong, Hua Gao, Xiaoge Liu

Funding acquisition: Lijia He, Guangcai Feng, Hua Gao

Methodology: Lijia He, Guangcai Feng

Software: Lijia He, Guangcai Feng

Validation: Lijia He, Guangcai Feng, Wenbin Xu, Yuedong Wang, Zhiqiang Xiong, Hua Gao, Xiaoge Liu

Writing – original draft: Lijia He

© 2023. The Authors.

This is an open access article under the terms of the Creative Commons Attribution-NonCommercial-NoDerivs License, which permits use and distribution in any medium, provided the original work is properly cited, the use is non-commercial and no modifications or adaptations are made.

Coseismic Kinematics of the 2023 Kahramanmaraş, Turkey Earthquake Sequence From InSAR and Optical Data

Lijia He^{1,2} , Guangcai Feng^{1,2} , Wenbin Xu^{1,2} , Yuedong Wang^{1,2} , Zhiqiang Xiong^{1,2}, Hua Gao³ , and Xiaoge Liu^{1,2} 

¹Laboratory of Radar Remote Sensing, School of Geosciences and Info-Physics, Central South University, Changsha, China,

²Key Laboratory of Metallogenetic Prediction of Nonferrous Metals and Geological Environment Monitoring, Central South University, Changsha, China, ³School of Geography and Environment, Jiangxi Normal University, Nanchang, China

Abstract We derive the ALOS-2 coseismic interferograms, pixel-offsets and Sentinel-2 sub-pixel offsets of the 2023 $M_w 7.8$ and $M_w 7.7$ Kahramanmaraş, Turkey earthquake sequence. Offset maps show that the sequence ruptured ~ 300 km along the East Anatolian Fault (EAF) and ~ 180 km along the secondary Cardak and Dogansehir faults. We infer the coseismic slip distribution and interseismic fault motion by inverting the co- and inter-seismic observations. Inversion results show that the coseismic slip (~ 8.0 m) and interseismic strike-slip rate (~ 4.6 mm/yr) on the main rupture of the $M_w 7.8$ event are basically consistent with the ~ 8.4 m and ~ 3.9 mm/yr of the $M_w 7.7$ event. Most coseismic slips of the $M_w 7.8$ and $M_w 7.7$ events occur within 10 and 12 km at depth, respectively, in keeping with the interseismic locking depth of 10.4 ± 3.3 km and 11.1 ± 3.1 km. This implies that the coseismic rupture kinematics correlate with the interseismic strain accumulation. Moreover, static stress changes show that the $M_w 7.7$ event is likely promoted by ~ 2 bar stress increase from the $M_w 7.8$ event on the central section of its main rupture.

Plain Language Summary The middle and northern sections of the East Anatolian Fault (EAF) have experienced seven major earthquakes ($M > 6.0$) since the twentieth century, in accordance with the fast slip rate (~ 10.5 mm/yr) and shallow locking depth (~ 5 km) (Bletery et al., 2020, <https://doi.org/10.1029/2020gl087775>), leaving a well-known seismic gap, the Pazarcık segment in the southern section of the EAF. Stress analysis by Nalbant et al. (2002, [https://doi.org/10.1016/s0016-821x\(01\)00592-1](https://doi.org/10.1016/s0016-821x(01)00592-1)) suggested that this seismic gap has potential to produce an $M_w \geq 7.3$ earthquake. The 2023 $M_w 7.8$ and $M_w 7.7$ Kahramanmaraş, Turkey earthquake sequence ruptured the Pazarcık segment. This earthquake sequence offers a valuable opportunity to explore the critical stage of the seismic cycle from interseismic strain accumulation to coseismic rupture. We extract the surface fault traces from the deformation maps derived from the ALOS-2 interferometric synthetic aperture radar (InSAR), pixel offset and Sentinel-2 sub-pixel offset measurements, and then construct a seven-segment fault geometric model according to the fault segmentation based on Duman and Emre (2013, <https://doi.org/10.1144/SP372.14>). By inverting the coseismic interferograms and pixel offsets and the interseismic LOS velocities from Weiss et al. (2020, <https://doi.org/10.1029/2020GL087376>), we determine the coseismic slip model of $M_w 7.8$ and $M_w 7.7$ earthquakes, and relate it to the interseismic kinematics.

1. Introduction

The East Anatolian Fault (EAF), located in southeastern Turkey, is a northeast-southwest trending and about 700 km long sinistral strike-slip fault. It regulates the relative movement between the Arabian and Anatolian blocks (Güvercin et al., 2022). It connects the tectonically active dextral North Anatolian Fault (NAF) to the northeast and borders on the sinistral Dead Sea Fault (DSF) to the southwest. Seven major earthquakes ($M > 6.0$) occurred here had broken some segments of the EAF since the twentieth century (Figure 1), leaving two seismic gaps (Duman & Emre, 2013). One is the Pütürge segment, on which the 2020 $M_w 6.8$ Sivrice earthquake broke a ~ 45 km long rupture (Konca et al., 2021). The other is the Pazarcık segment (longitude between 36.9°E and 37.7°E), the most potential segment to generate $M_w \geq 7.3$ destructive earthquakes as supposed by Nalbant et al. (2002) and Sunbul (2019) based on the Coulomb stress analysis.

The EAF trends northeastward between the Pazarcık and Palu segments, but trends north-northeastward on the Amanos segment. The strike-slip rate along the EAF decreases from 10 to 13 mm/yr on the Pütürge-Palu segment

Writing – review & editing: Lijia He,
Guangcai Feng

(east of 38.2°E) to 4~7 mm/yr on the Pazarcık-Erkenek segment (36.9°E–38.2°E) and then drop to 1~3 mm/yr on the Amanos segment (west of 36.9°E), according to some geological (e.g., Allen et al., 2004; Duman & Emre, 2013; Westaway, 1994, 2004) and geodetic (e.g., Aktug et al., 2016; Bletary et al., 2020; Cavalie & Jonsson, 2014; Reilinger et al., 2006; Walters et al., 2014) measurements. Such a decrease from northeast to southwest suggests that the interseismic strain accumulated on the main fault (e.g., Hussain et al., 2018; Weiss et al., 2020) is assigned to some large subsidiary faults (e.g., the Cardak fault). Therefore, some segments in the southwest of the EAF, such as the Amanos, Pazarcık, and Erkenek segments, have the potential to produce large earthquakes even though their long-term slip rate is low.

The 6 February 2023 Kahramanmaraş, Turkey earthquake sequence consists of three destructive left-lateral earthquakes in southeastern Turkey, close to the northern border of Syria, resulting in more than fifty thousand deaths in Turkey and Syria, where local roads and buildings were severely damaged. The earthquake sequence initiated at 1:17 a.m. (UTC time) with a M_w 7.8 devastating earthquake that broken the Amanos, Pazarcık, and Erkenek segments of the EAF (Figure 1). The surface rupture extends over 300 km along the northeast-southwest direction. About 11 min later (1:28 a.m., UTC time), an M_w 6.8 early aftershock occurred on the south-southwest trending, ~140 km long Amanos segment of the EAF. Approximately 9 hr after the M_w 7.8 event (10:24 a.m., UTC time), an M_w 7.7 earthquake, happened about 95 km northwest of the M_w 7.8 event. It struck the nearly east-west trending Cardak and northeast trending Doganşehir faults, two subsidiary faults with the surface rupture length of ~180 km. The occurrence of the 2023 Kahramanmaraş earthquake sequence filled the seismic gap on the Pazarcık segment.

The 2023 Kahramanmaraş earthquake sequence showed a synchronization phenomenon between the main fault segments of the EAF and nearby subsidiary faults. Earthquake synchronization within a short time interval (hours to days) has been observed in some strike-slip fault systems, such as the case for the 1987 Superstition Hills (e.g., Hudnut et al., 1989) and the 2019 Ridgecrest earthquake sequences (e.g., Barnhart et al., 2019; Ross et al., 2019), but it is rare in the EAF system. The Kahramanmaraş earthquake sequence offers a precious opportunity for using space-based geodetic data to understand the coseismic slip behaviors of such events, the interplay between co- and inter-seismic kinematics, and the influence of static stress transfer on rupture propagation.

In this study, we use InSAR and pixel-offset measurements of ALOS-2 SAR data and sub-pixel correlation of Sentinel-2 optical data to derive the complete coseismic deformation maps and constrain the coseismic fault geometries and kinematics of the 2023 Kahramanmaraş earthquakes. We compute the static stress changes on the seismogenic faults and nearby active faults based on the inferred slip model. We take the interseismic LOS velocity map around the seismogenic area from Weiss et al. (2020) for profile inversion, so as to investigate fault motion at depth. We make interpretations for the coseismic slip and discuss the interplay between the co- and inter-seismic kinematics.

2. Geodetic Data and Methods

The geodetic data sets are comprised of SAR and optical coseismic observations, and interseismic LOS velocity map across the southwest section of the EAF. The SAR data sets contain two ascending and two descending L-band ALOS-2 images (Table S1 in the Supporting Information S1). The optical data sets consist of nine pairs of Sentinel-2 images. The interseismic LOS velocity map is processed by Weiss et al. (2020).

To measure the line-of-sight (LOS) coseismic deformation maps of the 2023 Kahramanmaraş earthquakes, we process the ALOS-2 single look complex (SLC) images with the GAMMA software (Werner et al., 2000). In the differential InSAR (DInSAR) processing, we set 3 range and 16 azimuth looks. The Shuttle Radar Topographic Mission (SRTM) Digital Elevation Model (DEM) at 30 m resolution is used to coregister SLC image pairs and remove topographic phase in interferograms. The improved Goldstein filter method (Li et al., 2008) and the minimum cost flow method (Chen & Zebker, 2002) are used for filtering interferograms and unwrapping phase, respectively. We take the ascending images as an example to describe the detailed data processing strategy for the ALOS-2 Scanning SAR (ScanSAR) mode data (Text S1 in the Supporting Information S1). The derived ascending and descending ALOS-2 coseismic interferograms are shown in Figures 2a and 2e, respectively.

To obtain the pixel-offset maps of the 2023 Kahramanmaraş earthquakes, we utilize the pixel offset-tracking (POT) method to process the amplitude images of ALOS-2 data (Michel et al., 1999). The matching window size is set as 60 pixels in range and 320 pixels in azimuth with a moving step of 3×16 pixels. The range and azimuth offset maps are shown in Figures 2b, 2c, 2f, and 2g. We calculate the three-dimensional (3-D) deformation map of the 2023 Kahramanmaraş earthquakes by jointly using the two InSAR-derived LOS deformations and four

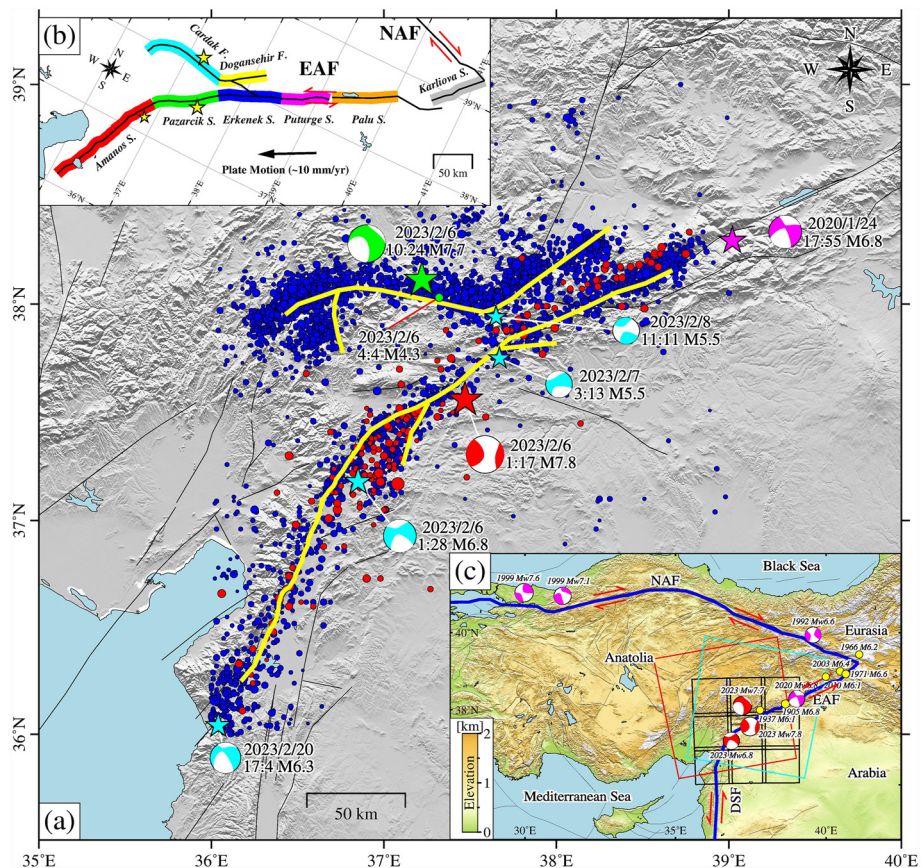


Figure 1. (a) Early aftershock distribution and surface fault traces of the 2023 Kahramanmaraş earthquake sequence. Red dots are the aftershocks occurred within the time span between the M_w 7.8 and M_w 7.7 events. Blue dots are the aftershocks occurred within the first month after the M_w 7.8 event recorded by the European Mediterranean Seismological Center (EMSC) (<https://www.emsc-csem.org/Earthquake/?filter=yes>). The green dot is an M4.3 aftershock happened after the M_w 7.8 event before the M_w 7.7 event. The moment magnitude of the second largest event in the 2023 Kahramanmaraş earthquake sequence is chosen as M_w 7.7 recorded by the Global Centroid Moment Tensor (GCMT; <https://www.globalcmt.org/CMTsearch.html>) rather than M_w 7.5 recorded by the U.S. Geological Survey (USGS; <https://earthquake.usgs.gov/earthquakes/map/>), because it is closer to the M_w 7.71 estimated from our geodetic data inversion (see Section 4). Yellow heavy lines are the surface fault traces extracted from the SAR and optical pixel offset maps (Figure 2). Black lines are the regional active fault lines from Styron & Paganini (2020). The red, green and cyan beach balls and stars are the focal mechanism solutions and epicentral locations of $M \geq 5.5$ events, respectively, given by the GCMT catalog. The magenta beach ball and star are the focal mechanism solutions and epicentral location of the 2020 M_w 6.8 Sivrice earthquake. (b) Fault segmentation along the East Anatolian Fault (EAF) marked by color-coded bands based on Duman and Emre (2013). (c) Historical major earthquakes around the Anatolian block since the twentieth century and the coverage of the space-based geodetic data used in this study. Yellow dots are the epicentral location of six $M > 6$ earthquakes recorded by the USGS catalog. Red and cyan boxes are the coverage of the ascending and descending ALOS-2 SAR data, respectively. The nine coverage of the Sentinel-2 data are marked by the black boxes and they are marked by different colors shown in Figure S1 in the Supporting Information S1.

POT-derived pixel offsets with a weighted least squares method (Hu et al., 2014). For simplicity, we utilize the uncertainties determined from the observations in the far-field non-deformed areas to weight different data sets (He, Feng, Li, et al., 2019). The derived 3-D deformation map is shown in Figures 2i–2k.

To measure the surface horizontal deformation map, we process the optical data by sub-pixel correlation (SPC) (e.g., Avouac et al., 2006; He et al., 2021). We cross-correlate the pre- and post-event Sentinel-2 images on Band 8 with the COSI-Corr software package (Leprince et al., 2007). We set the sliding window size, moving step and robustness iteration as 32×32 pixels, 3 pixels (~30 m resolution) and 4 times, respectively. To mitigate the systematic error sources in optical observations, we post-process the raw Sentinel-2 horizontal deformation maps in the east-west and north-south directions (Figures S5a and S5b in the Supporting Information S1). The long-wavelength orbital ramp is determined from the observations in the far-field stable areas and detrended by the bilinear polynomial curve fitting method. The stripe artifacts and attitude jitter distortions are eliminated by the improved mean subtracting method

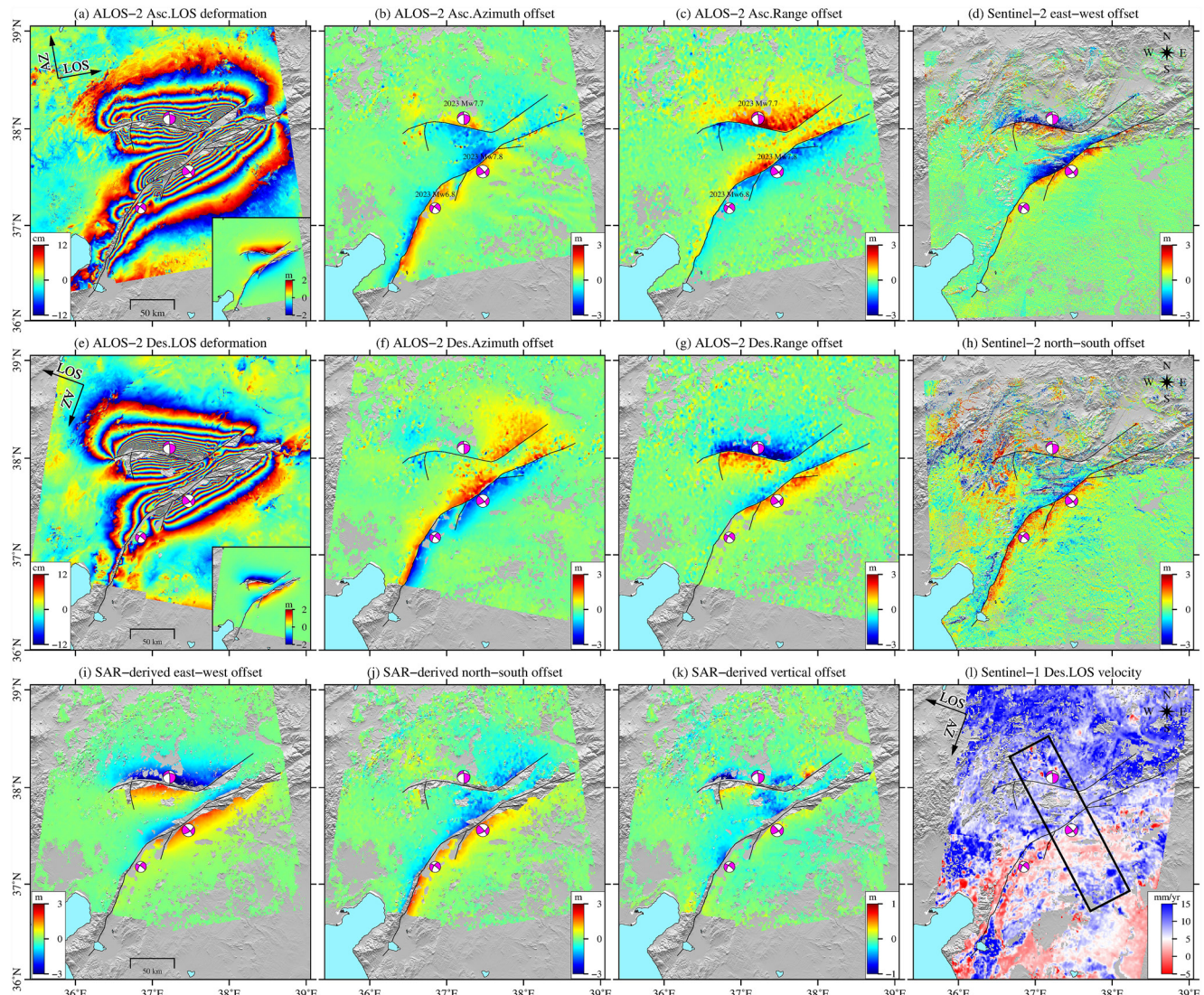


Figure 2. (a)–(k) Coseismic and (l) interseismic deformation maps of the 2023 Kahramanmaraş earthquake sequence. (a)–(c) are the ascending ALOS-2 line-of-sight (LOS) deformation, azimuth and range pixel offset maps, respectively. (e)–(g) are the same as (a)–(c) but for the descending ALOS-2 observations. (i)–(k) are the SAR-derived three-dimensional deformation maps. (d) and (h) are the Sentinel-2 east-west and north-south components of horizontal deformation, respectively. (l) is the Sentinel-1 descending (track 21) LOS velocity map from Weiss et al. (2020). The black box is the profile location with 200 km long and 50 km wide.

(He, Feng, Feng, et al., 2019). We mask out the observations with signal-to-noise ratio (SNR) below 0.9. The corrected east-west and north-south components of surface horizontal deformation are shown in Figures 2d and 2h.

3. Modeling Strategy

Given that the fault ruptures of the 2023 Kahramanmaraş earthquakes reach the surface according to the coseismic deformation measurements (Figure 2), we thus only carry out the linear inversion for the coseismic slip distribution. Before coseismic source modeling, to improve inversion efficiency, the InSAR-derived LOS deformations and POT-derived range and azimuth offsets are downsampled using the saliency-based quadtree sampling algorithm (Gao et al., 2021). To weight the downsampled data, we construct a variance-covariance matrix considering the noise structure (He et al., 2022). In addition, we perform interseismic profile inversion for strike-slip rate, dip-slip rate, locking depth and dip angle on the main seismogenic faults.

In coseismic source modeling, we establish a seven-segment (named F1–F7) geometric model with changeable fault strikes and dips according to the fault segmentation based on Duman and Emre (2013). The model is

constrained by the surface rupture traces extracted from offset maps (Figure 2). The strike- and dip-slip senses are constrained by the horizontal (Figures 2i and 2j) and vertical (Figure 2k) deformation patterns. We enlarge the down-dip depth to 30 km, and discretize the fault planes into a series of rectangle dislocations embedded in a uniform elastic half space (Okada, 1992). For the rectangle patches, we set a constant length (4 km) and an increasing width with depth by a factor of 1.4, because the patches located at deep depth are usually poorly constrained by geodetic data. The predefined dip bounds of each segment vary from 60°W to 60°E, except for segment F7 which vary from 50°S to 50°N. We set the dip increment as 1°, and explore the optimal value by a grid search method (Figure S6 in the Supporting Information S1). The second-order Laplace smoothing constraint is imposed to avoid oscillations of slip solution (Jónsson et al., 2002). To choose a proper smoothing factor, we test 30 different values that are equally divided in logarithmic form from 0.01 to 10 (Figure S7 in the Supporting Information S1). Based on the bounded variable least squares algorithm (Stark & Parker, 1995), we jointly invert the LOS and pixel-offset observations to simultaneously solve the coseismic slip distributions of the M_w 7.8 and M_w 7.7 earthquakes. In addition, we carry out slip uncertainty analysis and resolution tests to investigate the robustness and resolving power of the best-fitting slip model (Text S2 in the Supporting Information S1). We calculate the static Coulomb failure stress (CFS) changes on segments F1–F7 and the unbroken Sürgü fault between segments F3 and F6 based on the preferred coseismic slips on segments F1–F5 (Text S3 in the Supporting Information S1).

To investigate the interseismic fault motion at depth on the main rupture (i.e., Pazarcık fault; PF) of the M_w 7.8 event and that (i.e., Cardak fault; CF) of the M_w 7.7 event, we create a profile (200 km long and 50 km wide) that crosses the PF and CF. We extract the velocity profile from the Sentinel-1 descending (track 21) line-of-sight (LOS) velocity map processed by Weiss et al. (2020) (Figure 2l), and then invert it to estimate the strike-slip rate, dip-slip rate, locking depth and dip angle of each segment according to an adjusted elastic dislocation model. The detailed interseismic modeling strategy and uncertainty analysis are described in Texts S4 and S5 in the Supporting Information S1, respectively.

4. Inversion Results

The M_w 7.8 event is dominated by left-lateral strike-slip motions and accompanied by thrust dip-slip components. Most coseismic slips occur within 10 km depth (Figure 3). The maximum strike-slip/dip-slip motions on segments F1–F5 reach 5.2/1.7 m, 7.7/5.1 m, 7.6/2.1 m, 5.8/1.4 m, and 3.7/1.5 m, respectively. For the M_w 7.7 event, the main segment F6 is dominated by left-lateral strike-slip motions (up to 8.4 m) and accompanied by normal dip-slip components (up to 6 m) on its west section and thrust dip-slip components (up to 2 m) on its east section. Majority of coseismic slips are concentrated at 0~12 km depth. The branch segment F7 is dominated by pure normal dip-slip with a peak value of 1.5 m. The geodetic observations are well restored by the preferred coseismic slip model (Figures S14 and S15 in the Supporting Information S1). The LOS residual maps show a few deformation fringes near the fault rupture. The possible explanations include: (a) the delayed InSAR data acquisitions may have included early post-seismic deformation (e.g., afterslip), which could be solved together with the coseismic model in the kinematic inversion, but the poro- or visco-elastic processes cannot be modeled elastically; (b) the un-modeled small shallow structures near the rupture; (c) the plastic deformation or damaged surface near the rupture.

The entire geodetic moment generated by the coseismic slip on segments F1–F5 is about 5.30×10^{20} N m, corresponding to an M_w 7.78 earthquake (Table S2 in the Supporting Information S1). This is larger than the moment magnitude estimates of USGS (M_w 7.75), but smaller than that of GCMT (M_w 7.8). The geodetic moment released from the coseismic slip on the Pazarcık fault (i.e., segment F2) is 1.75×10^{20} N m, leading to an M_w 7.46 earthquake, which matches with the magnitude $M_w \geq 7.3$ earthquake speculated by Nalbant et al. (2002) and Sunbul (2019) based on the Coulomb stress analysis. The total geodetic moment produced by the coseismic slip on segments F6 and F7 is about 4.06×10^{20} N m, leading to an M_w 7.71 earthquake. This is consistent with the moment magnitude determined by GCMT (M_w 7.7), but larger than that inferred by USGS (M_w 7.55). The average dip angle (80°) of the main segments (F1–F3) of the M_w 7.8 event is larger than that (59°) of the main segment (F6) of the M_w 7.7 event. They are both at a compromise value between the dip angles given by USGS and GCMT (Table S3 in the Supporting Information S1). The average rake angles on segments F1–F3, and F6 are 6° and -4°, respectively, basically in consonance with the 11° and -8° recorded by GCMT.

5. Discussion

We compare the coseismic slip models of the 2023 Kahramanmaraş earthquakes with three other models (Barbot et al., 2023; Mai et al., 2023; U.S. Geological Survey, 2023) in terms of the fault geometry and coseismic slip

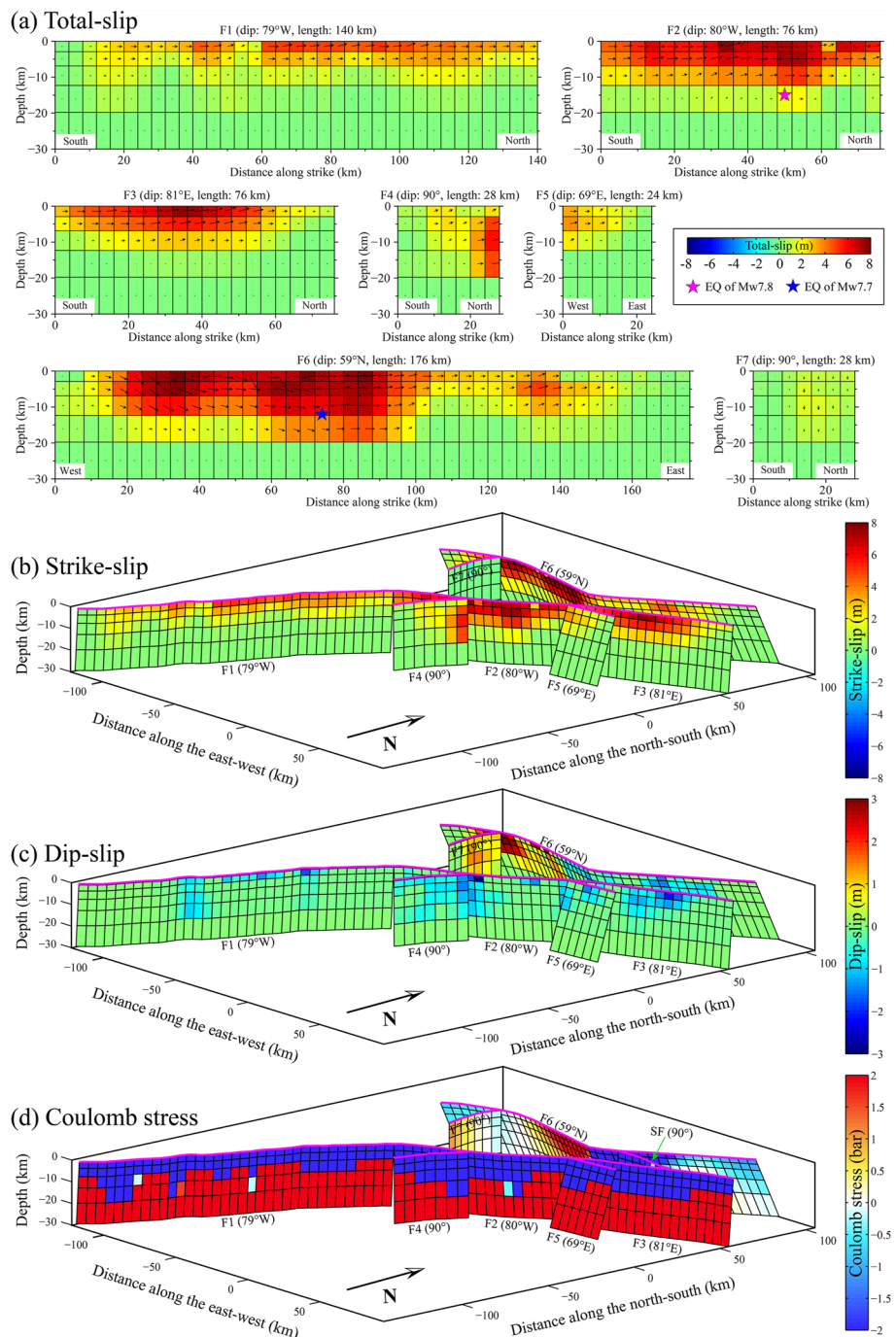


Figure 3. (a) Coseismic total-slip distribution of the $M_w 7.8$ event on segments F1–F5 and of the $M_w 7.7$ event on segments F6–F7 in the 2023 Kahramanmaraş earthquake sequence. Black arrows show the slip vectors. Magenta star on F2 and blue star on F6 are the epicentral location of the $M_w 7.8$ and $M_w 7.7$ events, respectively. (b)–(d) are the three-dimensional (3-D) view of the strike- and dip-slip distributions on F1–F7 and the Coulomb stress changes on F1–F7 and Sürgü fault (SF), respectively. The azimuth and elevation view angles are 50° and 15° , respectively.

distribution (Text S6 and Table S4 in the Supporting Information S1). Our inversion results are consistent with others, but show some obvious differences in the dip-slip on the main fault ruptures (i.e., Cardak and Dogansehir faults) of the $M_w 7.7$ event. The slip model of Barbot et al. (2023) indicated that no obvious dip-slip is seen on the Cardak fault (CF) and Dogansehir fault (DF). Their model shows a normal dip-slip (~ 1 m) on the Yeşilköy fault (i.e., segment F7), a NS-trending branch segment perpendicular to the CF. However, our results show that

the CF has different dip-slip sense on the bilateral side, its western and eastern sections have a normal dip-slip (up to 6 m) and a thrust dip-slip (up to 2 m), respectively (Figure S18 in the Supporting Information S1). Single releasing bend formed at a left-lateral strike-slip fault is often site of normal structures with transtensional deformation (Cunningham & Mann, 2007). This could explain the normal dip-slip motion in the western section of the CF. According to Duman and Emre (2013), a right fault stepover (~0.5 km-wide) exists in the Nurhak area of fault complexity (Figure S18 in the Supporting Information S1). It happens to be located in the place that divides the inferred dip-slip of the CF into two different senses. The sinistral strike-slip CF with such a right step-over usually produces transpressional deformation to form thrust structures (Oglesby, 2005). This could interpret the thrust dip-slip motion in the eastern section of the CF. In addition, we observe some thrust dip-slip components (up to 2 m) on the transpressional Dogansehir fault (Duman & Emre 2013). Compared with the ALOS-2 InSAR observations predicted by our preferred slip model (Figures S14 and S15 in the Supporting Information S1), Barbot et al. (2023) model has difficulties to fit the corresponding observations near the Dogansehir fault. It is likely due to the fact that their model has no obvious thrust dip-slip motion on this fault.

The intersecting fault in a fault network can limit rupture propagation of individual earthquake (e.g., Pizzi et al., 2017; Walters et al., 2018). We infer that the transverse unbroken Sürgü fault between segments F3 and F6 may act as a barrier to impede northeastward rupture propagation of the $M_w 7.8$ event. This inference can be validated by the following evidence. In a strike-slip faulting context, a slip curve that starts with gradual increase and ends with abrupt decrease has been recognized as a distinctive characteristic of a structural barrier that can stop seismic rupture suddenly (e.g., Klinger et al., 2006). Here, we find that the coseismic slip gradually increases northeastward from 2.9 to 7.6 m in ~36 km along the south part of segment F3 (Figure S19 in the Supporting Information S1). After passing through the interaction between segment F3 and the Sürgü fault, the coseismic slip abruptly decreases to 0.1 m in ~36 km along the north part of segment F3. We infer that a structural barrier is formed at the relay zone where the ruptured main fault has no direct physical contact with the unbroken subsidiary fault, which may be responsible for the rapid slip decrease.

We discuss the interplay between the inter- and co-seismic kinematics on the main ruptures of the 2023 Kahramanmaraş earthquakes. For the ~85 km long main segment (i.e., Cardak fault; CF) of the $M_w 7.7$ event, the inferred locking depth (11.1 ± 3.1 km) (Figure 4a) is in consonance with the rupture depth (0~12 km) where most coseismic slips distributed at (Figure 3a). For the ~82 km long main segment (i.e., Pazarcık fault; PF) of the $M_w 7.8$ event, the inferred locking depth (10.4 ± 3.3 km) is smaller than that of the CF. This is compatible with the shallower rupture depth (0~10 km) on the PF. Besides, the ratio of the interseismic strike-slip rate (4.6 ± 0.7 mm/yr vs. 3.9 ± 0.7 mm/yr) between the CF and PF is basically coincide with the ratio of the maximum coseismic slip (7.7 vs. 8.4 m). This suggests that the interseismic kinematics on the main ruptures of the 2023 Kahramanmaraş earthquakes show a good correlation with the coseismic slip behaviors.

We analyze the seismic moment variation from the interseismic strain accumulation to coseismic rupture. Given a fully locked fault, the CF has accumulated a slip deficit of 1.9 m since the previous M6.8 event in 1,544, leading to a moment deficit of 5.28×10^{19} N m ($M_w 7.12$), assuming the shear modulus, strike-slip rate, down-dip width and along-strike length of 30 GPa, 3.9 mm/yr, 11.1 and 85 km, respectively (Text S7 in the Supporting Information S1). Similarly, since the last M7.4 event in 1,513, the slip deficit and seismic moment accumulated on the PF are 2.3 m and 6.0×10^{19} N m, respectively, corresponding to an $M_w 7.15$ earthquake. The seismic moment deficit calculations show that the ratio between the seismic moment on the CF and PF accumulated in the interseismic period is almost consistent with the 2.51×10^{20} N m ($M_w 7.56$) and 1.75×10^{20} N m ($M_w 7.46$) released by the coseismic rupture. This suggests that the interseismic strain accumulation on the CF and PF is almost the same proportion as that released by the coseismic rupture. The interseismic accumulated seismic moment on individual segments is underestimated as it is smaller than the coseismic rupture released. This is likely due to that these segments are not completely relocked since the last earthquakes.

Fault failure can be affected by the seismic cycle effect, that is, whether a fault is close to the terminus of the seismic cycle. Scholz (2010) suggested that adjacent faults with similar interseismic slip rates can rupture synchronously. They suggested a possible physical mechanism for the fault synchronization: the long term (decades or longer) dynamic stress transfer on surrounding faults brings their seismic cycle to the end simultaneously. In the 2023 Kahramanmaraş earthquake sequence, similar interseismic slip rates (~4.6 mm/yr vs. ~3.9 mm/yr) are inferred on the main ruptures (i.e., PF and CF) of the $M_w 7.8$ and $M_w 7.7$ events. This provides favorable conditions for the synchronization of the two events. Compared with the North Anatolian fault, the seismogenic faults of this

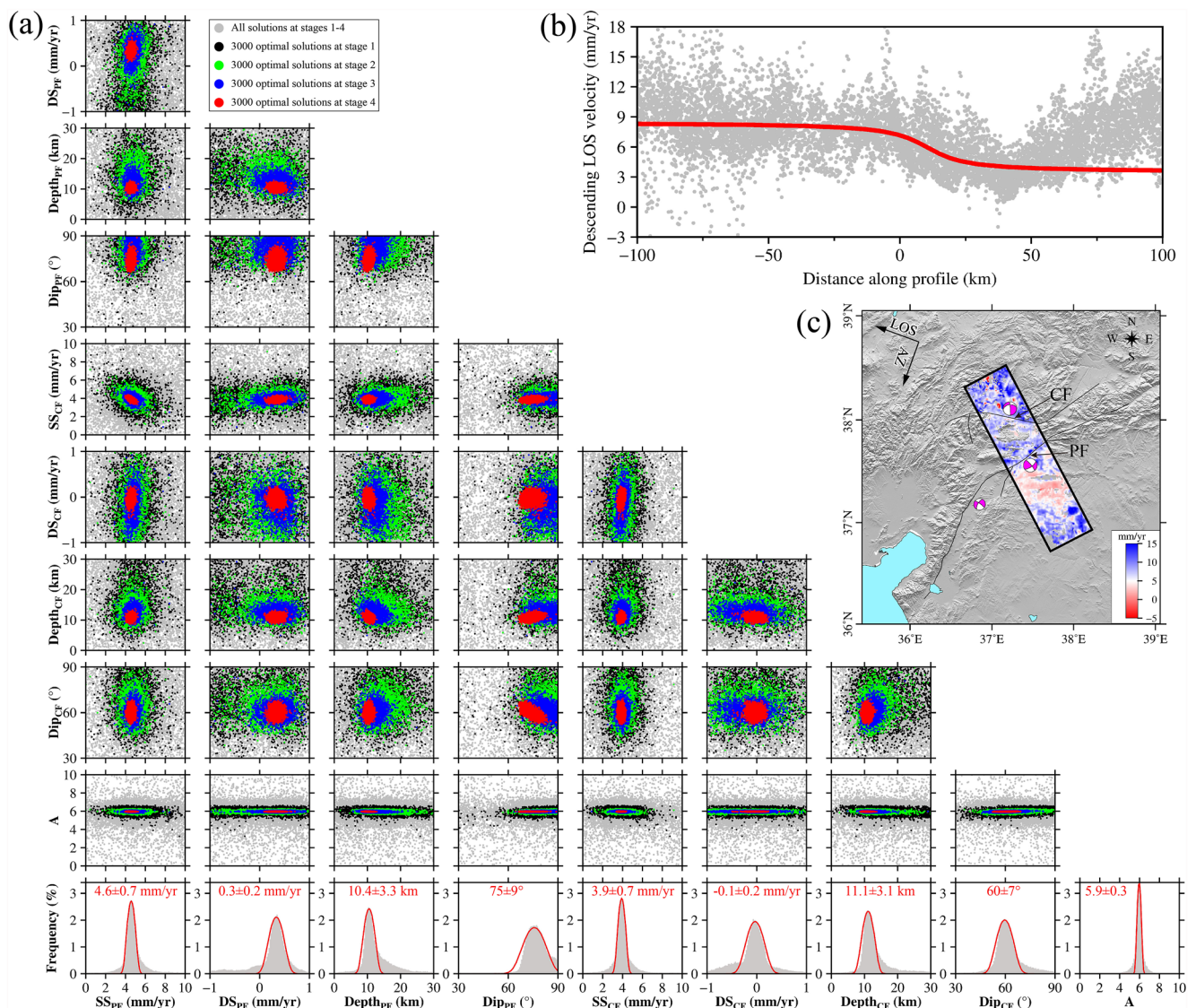


Figure 4. (a) The trade-off relationship of the strike-slip rate (SS), dip-slip rate (DS), locking depth (D) and fault dip (δ) between the Pazarcık fault (PF) and Cardak fault (CF). The inferred mean and uncertainty values of individual parameters are labeled in red in the corresponding histograms. The 96,200 solutions of each parameter obtained from stages 1–4 are shown by gray dots. The 3,000 optimal solutions with small misfits obtained from stages 1, 2, 3, and 4 are color coded by black, green, blue and red dots, respectively. (b) The Sentinel-1 descending line-of-sight (LOS) velocities within the profile marked by the black box in (c). All velocity points in the profile are shown by gray dots. The red line is fitted by the preferred interseismic model.

earthquake sequence have relatively low interseismic slip rate and strain accumulation, but still have the possibility to cause large earthquakes. The fault synchronization of this earthquake sequence suggest that more attention should be paid to the potential seismic disasters on the fault groups with low slip rate.

Static Coulomb stress transfer after a destructive earthquake may further trigger large earthquake on surrounding active faults. Given the hypothetical earthquake triggering threshold of 0.1~0.5 bar (Hardebeck et al., 1998; King et al., 1994), the M_w 7.7 event is likely brought to the brink of failure by ~2 bar positive stress change on the central section of segment F6 generated by the M_w 7.8 event (Figure 3d). We also observe that the unbroken Sürgü fault experienced the stress shadow (~2 bar) caused by the M_w 7.8 event, which may arrest the rupture and minimize the possibility of triggering earthquake along this fault. The stress triggering relationship between two main events with short time interval can also been found in other strike-slip fault systems. Such as the 2019 Ridgecrest earthquake sequence, the stress perturbation due to the M_w 6.4 foreshock appears to be responsible for the rupture of the M_w 7.1 mainshock ~34 hr latter (e.g., Barnhart et al., 2019). The aforementioned triggering threshold is

controversial (Ziv & Rubin, 2000) and it is not considered in some studies on Coulomb stress triggering (e.g., Mildon et al., 2019; Wang et al., 2014). Mildon et al. (2019) introduced two measures (i.e., the proportion of fault with positive CFS and the peak magnitude of CFS on fault) to evaluate the earthquake triggering hypothesis. Wang et al. (2014) related the magnitude of CFS changes to the advance or delay of earthquake recurrence time. These studies used different strategies to evaluate the potential earthquake risks, and their combined effects should be considered in regional seismic hazard assessment.

6. Conclusions

We determine the detailed coseismic slip distribution of the 2023 Kahramanmaraş earthquakes by jointly inverting the near-field pixel offsets and the intermediate-field LOS deformations. Inversion results show that both the M_w 7.8 and M_w 7.7 events are dominated by the sinistral strike-slip motion, and the former is accompanied with the thrust dip-slip motion along the main rupture, and the latter with the normal dip-slip motion in the western section and the thrust dip-slip motion in the eastern section of the Cardak fault (CF). Coseismic slip interpretation shows that the Sürgü fault (SF) may act as a barrier to impede northeastward rupture propagation of the M_w 7.8 event. We analyze the interplay between the inter- and co-seismic kinematics along the CF and Pazarcık fault (PF). Analysis results indicate that the coseismic slip behaviors correlate with the interseismic kinematics, and the interseismic strain accumulation on the CF and PF is almost the same proportion as that released by the coseismic rupture. Similar strike-slip rates are inferred on the CF and PF, which may play a role in expediting synchronization of the M_w 7.8 and M_w 7.7 events. Coulomb stress calculation results show that the SF and the epicenter of the M_w 7.7 event experience stress decrease and increase caused by the M_w 7.8 event, respectively, suggesting that the M_w 7.8 event may arrest the rupture on the SF and brought the M_w 7.7 event to the brink of failure.

Data Availability Statement

The aftershocks of the 2023 Kahramanmaraş earthquake sequence come from the European Mediterranean Seismological Center (EMSC) (<https://www.emsc-csem.org/Earthquake/?filter=yes>). The ALOS-2/PALSAR-2 data used in this study are publicly downloaded from https://www.eorc.jaxa.jp/ALOS/jp/dataset/open_and_free/JAXA_ALOS-2_PALSAR-2_ScanSAR_turkey_L1.1_Link_20230228.html.

Acknowledgments

The authors thank the editor Lucy Flesch, Xiaohua Xu, and an anonymous reviewer for their thoughtful and thorough comments that greatly improved this manuscript. This work was supported by the National Natural Science Foundation of China (No. 42174039), the Scientific Research Innovation Project for Graduate Students in Hunan Province (No. CX20210105), the Fundamental Research Funds for the Central Universities of Central South University (No. 2021zzts0250), and the Key Research and Development Program Project of Jiangxi Province (No. 2023B0BE00021). The figures in this work were generated by the Generic Mapping Tools (Wessel et al., 2013).

References

- Aktug, B., Ozener, H., Dogru, A., Sabuncu, A., Turgut, B., Halicioglu, K., et al. (2016). Slip rates and seismic potential on the East Anatolian Fault System using an improved GPS velocity field. *Journal of Geodynamics*, 94–95, 1–12. <https://doi.org/10.1016/j.jog.2016.01.001>
- Allen, M., Jackson, J., & Walker, R. (2004). Late Cenozoic reorganization of the Arabia-Eurasia collision and the comparison of short-term and long-term deformation rates. *Tectonics*, 23(2), TC2008. <https://doi.org/10.1029/2003TC001530>
- Avouac, J. P., Ayoub, F., Leprince, S., Konca, O., & Helberger, D. V. (2006). The 2005, Mw 7.6 Kashmir earthquake: Sub-pixel correlation of aster images and seismic waveforms analysis. *Earth and Planetary Science Letters*, 249(3–4), 514–528. <https://doi.org/10.1016/j.epsl.2006.06.025>
- Barbot, S., Luo, H., Wang, T., Hamiel, Y., Piatibratova, O., Javed, M. T., et al. (2023). Slip distribution of the February 6, 2023 Mw 7.8 and Mw 7.6, Kahramanmaraş, Turkey earthquake sequence in the East Anatolian fault zone. *Seismica*, 2(3). <https://doi.org/10.26443/seismica.v2i3.502>
- Barnhart, W. D., Hayes, G. P., & Gold, R. D. (2019). The July 2019 ridgecrest, California, earthquake sequence: Kinematics of slip and stressing in cross-fault ruptures. *Geophysical Research Letters*, 46(21), 11859–11867. <https://doi.org/10.1029/2019GL084741>
- Bleiter, Q., Cavalie, O., Nocquet, J. M., & Ragon, T. (2020). Distribution of interseismic coupling along the North and East Anatolian faults inferred from InSAR and GPS data. *Geophysical Research Letters*, 47(16), e2020GL087775. <https://doi.org/10.1029/2020GL087775>
- Cavalie, O., & Jónsson, S. (2014). Block-like plate movements in eastern Anatolia observed by InSAR. *Geophysical Research Letters*, 41(1), 26–31. <https://doi.org/10.1002/2013GL058170>
- Chen, C. W., & Zebker, H. A. (2002). Phase unwrapping for large SAR interferograms: Statistical segmentation and generalized network models. *IEEE Transactions on Geoscience and Remote Sensing*, 40(8), 1709–1719. <https://doi.org/10.1109/TGRS.2002.802453>
- Cunningham, W. D., & Mann, P. (2007). Tectonics of strike-slip restraining and releasing bends. *Geological Society, London, Special Publications*, 290(1), 1–12. <https://doi.org/10.1144/SP290.1>
- Duman, T. Y., & Emre, Ö. (2013). The East Anatolian fault: Geometry, segmentation and jog characteristics. *Geological Society, London, Special Publications*, 372(1), 495–529. <https://doi.org/10.1144/SP372.14>
- Gao, H., Liao, M., & Feng, G. (2021). An improved quadtree sampling method for InSAR seismic deformation inversion. *Remote Sensing*, 13(9), 1678. <https://doi.org/10.3390/rs13091678>
- Güvercin, S. E., Karabulut, H., Konca, A. Ö., Doğan, U., & Ergintav, S. (2022). Active seismotectonics of the East Anatolian fault. *Geophysical Journal International*, 230(1), 50–69. <https://doi.org/10.1093/gji/ggac045>
- Hardebeck, J. L., Nazareth, J. J., & Hauksson, E. (1998). The static stress change triggering model: Constraints from two southern California aftershock sequences. *Journal of Geophysical Research*, 103(B10), 24427–24437. <https://doi.org/10.1029/98JB00573>
- He, L., Feng, G., Feng, Z., & Gao, H. (2019). Coseismic displacements of 2016 Mw 7.8 Kaikoura, New Zealand earthquake, using sentinel-2 optical images. *Acta Geodaetica et Cartographica Sinica*, 48(3), 339. <https://doi.org/10.11947/j.AGCS.2019.20170671>

- He, L., Feng, G., Hu, J., Xu, W., Liu, J., Li, Z., et al. (2022). Surface displacement and source model separation of the two strongest earthquakes during the 2019 ridgecrest sequence: Insights from InSAR, GPS, and optical data. *Journal of Geophysical Research: Solid Earth*, 127(2), e2021JB022779. <https://doi.org/10.1029/2021JB022779>
- He, L., Feng, G., Li, Z., Feng, Z., Gao, H., & Wu, X. (2019). Source parameters and slip distribution of the 2018 Mw 7.5 Palu, Indonesia earthquake estimated from space-based geodesy. *Tectonophysics*, 772, 228216. <https://doi.org/10.1016/j.tecto.2019.228216>
- He, L., Feng, G., Wu, X., Lu, H., Xu, W., Wang, Y., et al. (2021). Coseismic and early postseismic slip models of the 2021 Mw7.4 Madou earthquake (western China) estimated by space-based geodetic data. *Geophysical Research Letters*, 48, e2021GL095860. <https://doi.org/10.1029/2021GL095860>
- Hu, J., Li, Z. W., Ding, X. L., Zhu, J. J., Zhang, L., & Sun, Q. (2014). Resolving three-dimensional surface displacements from InSAR measurements: A review. *Earth-Science Reviews*, 133, 1–17. <https://doi.org/10.1016/j.earscirev.2014.02.005>
- Hudnut, K. W., Seeber, L., & Pacheco, J. (1989). Cross-fault triggering in the November 1987 superstition hills earthquake sequence, southern California. *Geophysical Research Letters*, 16(2), 199–202. <https://doi.org/10.1029/GL016i002p00199>
- Hussain, E., Wright, T. J., Walters, R. J., Bekaert, D. P., Lloyd, R., & Hooper, A. (2018). Constant strain accumulation rate between major earthquakes on the North Anatolian fault. *Nature Communications*, 9(1), 1392. <https://doi.org/10.1038/s41467-018-03739-2>
- Jónsson, S., Zebker, H., Segall, P., & Amelung, F. (2002). Fault slip distribution of the 1999 Mw7.1 hector mine, California, earthquake, estimated from satellite radar and GPS measurements. *Bulletin of the Seismological Society of America*, 92(4), 1377–1389. <https://doi.org/10.1785/0120000922>
- King, G. C., Stein, R. S., & Lin, J. (1994). Static stress changes and the triggering of earthquakes. *Bulletin of the Seismological Society of America*, 84(3), 935–953. <https://doi.org/10.1785/BSSA0840030935>
- Klinger, Y., Michel, R., & King, G. C. (2006). Evidence for an earthquake barrier model from Mw~7.8 Kokoxili (Tibet) earthquake slip-distribution. *Earth and Planetary Science Letters*, 242(3–4), 354–364. <https://doi.org/10.1016/j.epsl.2005.12.003>
- Konca, A. Ö., Karabulut, H., Güvercın, S. E., Eskiköy, F., Özarpaci, S., Özdemir, A., et al. (2021). From interseismic deformation with near-repeating earthquakes to co-seismic rupture: A unified view of the 2020 Mw6.8 Sivrice (elazığ) eastern Turkey earthquake. *Journal of Geophysical Research: Solid Earth*, 126(10), e2021JB021830. <https://doi.org/10.1029/2021JB021830>
- Leprince, S., Barbot, S., Ayoub, F., & Avouac, J. P. (2007). Automatic and precise orthorectification, coregistration, and subpixel correlation of satellite images, application to ground deformation measurements. *IEEE Transactions on Geoscience and Remote Sensing*, 45(6), 1529–1558. <https://doi.org/10.1109/tgrs.2006.888937>
- Li, Z. W., Ding, X. L., Huang, C., Zhu, J. J., & Chen, Y. L. (2008). Improved filtering parameter determination for the goldstein radar interferogram filter. *ISPRS Journal of Photogrammetry and Remote Sensing*, 63(6), 621–634. <https://doi.org/10.1016/j.isprsjprs.2008.03.001>
- Mai, P. M., Aspiotis, T., Aquib, T. A., Cano, E. V., Castro-Cruz, D., Espindola-Carmona, A., et al. (2023). The destructive earthquake doublet of 6 February 2023 in south-central Türkiye and northwestern Syria: Initial observations and analyses. *The Seismic Record*, 3(2), 105–115. <https://doi.org/10.1785/0320230007>
- Michel, R., Avouac, J. P., & Taboury, J. (1999). Measuring near field coseismic displacements from SAR images: Application to the landers earthquake. *Geophysical Research Letters*, 26(19), 3017–3020. <https://doi.org/10.1029/1999GL900524>
- Mildon, Z. K., Roberts, G. P., Faure Walker, J. P., & Toda, S. (2019). Coulomb pre-stress and fault bends are ignored yet vital factors for earthquake triggering and hazard. *Nature Communications*, 10(1), 1–9. <https://doi.org/10.1038/s41467-019-10520-6>
- Nalbant, S. S., McCloskey, J., Steacy, S., & Barka, A. A. (2002). Stress accumulation and increased seismic risk in eastern Turkey. *Earth and Planetary Science Letters*, 195(3–4), 291–298. [https://doi.org/10.1016/S0012-821X\(01\)00592-1](https://doi.org/10.1016/S0012-821X(01)00592-1)
- Oglesby, D. D. (2005). The dynamics of strike-slip step-overs with linking dip-slip faults. *Bulletin of the Seismological Society of America*, 95(5), 1604–1622. <https://doi.org/10.1785/0120050058>
- Okada, Y. (1992). Internal deformation due to shear and tensile faults in a half-space. *Bulletin of the Seismological Society of America*, 82(2), 1018–1040. <https://doi.org/10.1785/BSSA0820201018>
- Pizzi, A., Di Domenica, A., Gallović, F., Luzi, L., & Puglia, R. (2017). Fault segmentation as constraint to the occurrence of the main shocks of the 2016 central Italy seismic sequence. *Tectonics*, 36(11), 2370–2387. <https://doi.org/10.1002/2017TC004652>
- Reilinger, R., McClusky, S., Vernant, P., Lawrence, S., Ergintav, S., Cakmak, R., et al. (2006). GPS constraints on continental deformation in the Africa-Arabia-Eurasia continental collision zone and implications for the dynamics of plate interactions. *Journal of Geophysical Research*, 111(B5), B05411. <https://doi.org/10.1029/2005JB004051>
- Ross, Z. E., Idini, B., Jia, Z., Stephenson, O. L., Zhong, M., Wang, X., et al. (2019). Hierarchical interlocked orthogonal faulting in the 2019 ridgecrest earthquake sequence. *Science*, 366(6463), 346–351. <https://doi.org/10.1126/science.aaz0109>
- Scholz, C. H. (2010). Large earthquake triggering, clustering, and the synchronization of faults. *Bulletin of the Seismological Society of America*, 100(3), 901–909. <https://doi.org/10.1785/0120090309>
- Stark, P. B., & Parker, R. L. (1995). Bounded-variable least-squares: An algorithm and applications. *Computational Statistics*, 10, 129.
- Styron, R., & Pagani, M. (2020). The GEM global active faults database. *Earthquake Spectra*, 36, 160–180. <https://doi.org/10.1177/8755293020944182>
- Sunbul, F. (2019). Time-dependent stress increase along the major faults in eastern Turkey. *Journal of Geodynamics*, 126, 23–31. <https://doi.org/10.1016/j.jog.2019.03.001>
- U. S. Geological Survey USGS (2023). Earthquake catalog released by U. S. Geological Survey. Retrieved from <https://earthquake.usgs.gov/earthquakes/eventpage/us6000jlz/> and <https://earthquake.usgs.gov/earthquakes/eventpage/us6000jlqa/>
- Walters, R. J., Gregory, L. C., Wedmore, L. N., Craig, T. J., McCaffrey, K., Wilkinson, M., et al. (2018). Dual control of fault intersections on stop-start rupture in the 2016 central Italy seismic sequence. *Earth and Planetary Science Letters*, 500, 1–14. <https://doi.org/10.1016/j.epsl.2018.07.043>
- Walters, R. J., Parsons, B., & Wright, T. J. (2014). Constraining crustal velocity fields with InSAR for eastern Turkey: Limits to the block-like behavior of eastern Anatolia. *Journal of Geophysical Research: Solid Earth*, 119(6), 5215–5234. <https://doi.org/10.1002/2013JB010909>
- Wang, Y., Wang, F., Wang, M., Shen, Z. K., & Wan, Y. (2014). Coulomb stress change and evolution induced by the 2008 Wenchuan earthquake and its delayed triggering of the 2013 Mw6.6 Lushan earthquake. *Seismological Research Letters*, 85(1), 52–59. <https://doi.org/10.1785/0220130111>
- Weiss, J. R., Walters, R. J., Morishita, Y., Wright, T. J., Lazecky, M., Wang, H., et al. (2020). High-resolution surface velocities and strain for Anatolia from sentinel-1 InSAR and GNSS data. *Geophysical Research Letters*, 47(17), e2020GL087376. <https://doi.org/10.1029/2020GL087376>
- Werner, C., Wegmüller, U., Strozzi, T., & Wiesmann, A. (2000). Gamma SAR and interferometric processing software. *Proceedings of the ers-envisat symposium*, 1620. Retrieved from <https://api.semanticscholar.org/CorpusID:28598270>
- Wessel, P., Smith, W. H., Scharrroo, R., Luis, J., & Wobbe, F. (2013). Generic mapping tools: Improved version released. *Eos, Transactions American Geophysical Union*, 94(45), 409–410. <https://doi.org/10.1002/2013eo450001>

- Westaway, R. (1994). Present-day kinematics of the middle east and eastern Mediterranean. *Journal of Geophysical Research*, 99(B6), 12071–12090. <https://doi.org/10.1029/94JB00335>
- Westaway, R. (2004). Kinematic consistency between the dead sea fault zone and the neogene and quaternary left-lateral faulting in SE Turkey. *Tectonophysics*, 391(1–4), 203–237. <https://doi.org/10.1016/j.tecto.2004.07.014>
- Ziv, A., & Rubin, A. M. (2000). Static stress transfer and earthquake triggering: No lower threshold in sight? *Journal of Geophysical Research*, 105(B6), 13631–13642. <https://doi.org/10.1029/2000jb900081>